Supplementary Materials for

Structure and membrane remodeling activity of ESCRT-III helical polymers

John McCullough[1,#], Amy K. Clippinger[2,#], Nathaniel Talledge[1,3], Michael L. Skowyra[2], Marissa G. Saunders[1], Teresa V. Naismith[2], Leremy A. Colf[1], Pavel Afonine[4], Christopher Arthur[5], Wesley I. Sundquist[1]*, Phyllis I. Hanson[2]*, and Adam Frost[1,3]*

correspondence to: wes@biochem.utah.edu (WIS), phanson22@wustl.edu (PIH), and adam.frost@ucsf.edu (AF)

This PDF file includes:

Other Supplementary Materials for this manuscript includes the following:

Materials and Methods

Protein Expression and Purification

CHMP1B and $IST1_{NTD}$ constructs were expressed and purified as described previously (4). Two slightly different sequences of CHMP1B have been reported (32, 33), which differ in the residue at position 34 (Asp vs. Lys), and are here termed CHMP1B and $CHMP1B_{34K}$. Both CHMP1B proteins form equivalent co-polymers with IST1. IST1 was expressed with an N-terminal His affinity tag in BL21 (DE3)- RIPL E. coli grown in auto-induction media ZYP-5052 (34) (6 L cultures). Cells were grown at 37 ºC for 6 hours with vigorous shaking in baffled flasks, moved to 19 ºC and grown for an additional 16-18 hours. Subsequent purification steps were performed at 4 ºC, except where noted. Cells were lysed by sonication, with lysozyme and sodium deoxycholate treatment (50 mM Tris, pH 7.5, 1 M NaCl, 10 mM Imidazole, 5% (w/v) glycerol, 5 mM beta-mercaptoethanol (BME)). The supernatant was clarified by centrifugation (37,000 g, 45 mins), filtered, and incubated with cOmplete His-Tag Purification Resin (Roche) for 1 hour. The bound protein was washed extensively with lysis buffer without lysozyme or sodium deoxycholate and eluted with 50 mM Tris, pH 7.5, 1 M NaCl, 750 mM Imidazole, 5% (w/v) glycerol, 5 mM BME. The eluted protein (~70 mL) was dialyzed stepwise against 20 mM Tris, pH 8.0, 1 M NaCl, 5 mM EDTA, 5% (w/v) glycerol (4 h, 23 ºC) and then 20 mM Tris, pH 8.0, 250 mM NaCl, 5% (w/v) glycerol, 5mM BME (4 h, 23 ºC). The affinity tag was removed by incubation with TEV protease (0.6 mg per 70 ml, 24 h, 23 ºC). The processed protein was dialyzed against Q column loading buffer (50 mM Tris, pH 8.0, 100 mM NaCl, 10 mM Imidazole, 5% (w/v) glycerol, 5 mM BME, 4 h), and incubated with cOmplete His-Tag Purification Resin (Roche) to remove residual His-IST1 (30 min). The flow-through was applied to a Q Sepharose Fast Flow column (GE Healthcare), washed with loading buffer, and eluted with a gradient from 100 mM NaCl to 250 mM NaCl in 50 mM Tris, pH 8.0, 10mM Imidazole, 5% (w/v) glycerol, 5 mM BME. Monomeric IST1 was isolated by gel filtration chromatography in 50 mM Tris, pH 8.0, 300 mM NaCl, 5% (w/v) glycerol, 5 mM BME on a HiLoad 16/60 Superdex S75 column (GE Healthcare). Protein identities were confirmed by mass spectrometry (CHMP1B: MW_{Calc}=21,972 Da, MW_{Exp}=21,971 Da; $CHMP1B_{K34}$: MW_{Calc}=21,971 Da, MWExp=21,971 Da; $CHMP1B_{K107D,D155R}$: MW_{Calc}=22,000 Da, MW_{Exp}=22,001 Da; $IST1_{NTD}$: MW_{Calc}=21,737 Da, MW_{Exp}=21,736 Da; $IST1_{NTD,R16E\ K27E}$: MW_{Calc}=21,711 Da, MW_{Exp}=21,711 Da; $IST1_{NTD,D42A}$: MW_{Calc}=21,692 Da, MW_{Exp}=21, 693 Da; $IST1_{NTD,I54D}$: MW_{Calc}=21,738 Da, MW_{Exp}=21,738 Da; $IST1_{NTD,K134D}$: MW_{Calc}=21,723 Da, MW_{Exp}=21,723 Da; $IST1_{NTD,N174D}$: MW_{Calc}=21,693 Da, MW_{Exp}=21,692 Da; IST1: MW_{Calc}=40,173 Da, MW_{Exp}=40,177 Da). Yields were ~ 45 mg for $IST1_{NTD}$ constructs, ~ 1 mg for CHMP1B constructs and ~ 18 mg for IST1 from 6 L cultures.

Analytical Ultracentrifugation

Four concentrations of CHMP1B (1.6 mM, 800 μM, 400 μM, 200 μM) were centrifuged to equilibrium at 12,000, 16,000, 20,000, and 24,000 RPM, in 20 mM NaPi, pH 7.0, 100 mM NaCl, 4°C. Absorbance data were recorded at 235 nm, with the two highest concentrations in 3 mm path length centerpieces and the lowest two in 12 mm

path length centerpieces. The data were globally fit with floating molecular weight to an ideal single species model using the nonlinear least squared algorithm in HeteroAnalysis (35). Protein partial specific volume and buffer density were calculated using SEDNTERP (36). The experimentally estimated molecular weight was 21,913 Da, in excellent agreement with the calculated monomeric molecular weight (21,972 Da); $MW_{Exp}/MW_{Calc} = 1.00$. Thus, CHMP1B is a monomer at these concentrations and solution conditions, but polymerizes spontaneously under lower ionic strength conditions.

SUV and Liposome Preparation

Stock lipid solutions (Avanti Polar Lipids) were resuspended in chloroform. To produce 37 mole % PS SUVs (37% phosphatidylserine (PS), 44% phosphatidylcholine (PC), 18% cholesterol, <1 % rhodamine-phosphatidylethanolamine (RhPE)), 2 mg total lipid were dried in a glass vial at room temperature under streaming nitrogen with vortexing. The thin lipid film was then dessicated in vacuo for 1 hour to remove residual chloroform. The lipids were re-dissolved in absolute hexane, dried under streaming nitrogen and dessicated in vacuo (4 hours). The lipid films were dispersed in 1 ml buffer (25 mM HEPES, pH 7.5, 150 mM KCl, 2 mg/ml final concentration, 23 ºC overnight with gentle rocking). The resuspended liposomes were subsequently extruded 50 times (Avanti Mini-Extruder) through 0.2 μm polycarbonate membranes. Liposomes, including an endosome-like combination of 30% PS, 35% PE, 30% PC, 5% Phosphatidylinositol 3-phosphate (PI(3)P) at a final concentration of 1 mg/ml with 100 mM NaCl and 50 mM Tris pH 7.5 buffer, were produced in a similar manner but were not subjected to extrusion. Liposomes and SUVs were stored at -80 ºC.

Membrane-free IST1 and CHMP1B Polymers

IST1, $IST1_{NTD}$, and CHMP1B (32 μM final protein concentrations) were incubated (or coincubated) in high ionic strength buffer (50 mM Tris, pH 7.0, 350 mM NaCl, 5% (w/v) glycerol, 5 mM BME, 100 μl volume) for 1 hour at 23 ºC in the presence or absence of 1 mg/ml 37% PS nucleating SUV's. Reactions were then dialyzed (10,000 MWCO, Slide-A-Lyzer MINI Dialysis Units, Thermo Scientific) against 1L low ionic strength buffer (25 mM Tris, pH 8.0, 25 mM NaCl, 23 ºC, 12 h). The assemblies were concentrated by low speed centrifugation (2,300 g, 5 min) and re-suspended in 10 μl low ionic strength buffer.

IST1 and CHMP1B Membrane Remodeling Reactions

Membrane remodeling reactions were performed at room temperature with total protein concentrations ranging from 2-30 μM and protein-to-lipid ratios from 1:0.2 to 1: 2.5 (mass:mass) at 100 mM NaCl concentration. For the reactions imaged in Figure 4 and Supplemental Figure S10-11, CHMP1B (5 μM final protein concentration) was incubated in medium ionic strength buffer (50 mM Tris, pH 7.5, 100 mM NaCl) with 30% PS liposomes at room temperature. $IST1_{NTD}$ (5 μM final protein concentration) was then added to the preformed CHMP1B membrane tubules in 100 μL reaction volumes for a final protein concentration of 10 μM. Total protein to lipid ratio was 1:2.3 by mass. The assemblies were concentrated by low speed centrifugation (2,300 g, 5 min) and re-suspended in 30 μl. CHMP1B-only reactions employed the same procedure using 10 μM CHMP1B without subsequent addition of IST1.

Negative Stain Electron Microscopy

SUV-nucleated copolymers of $IST1_{NTD}$-CHMP1B were prepared for TEM following established procedures (37, 38). Specifically, for imaging at the University of Utah, assembly reactions (4 µl) were applied to glow-discharged (PELCO EasiGlow, 15 mA, 0.39 mBar, 25 seconds) continuous carbon film grids (Formvar/Carbon Film (FCF-200-Cu)) and stained with saturated uranyl acetate. Negatively stained grids were imaged on a JEM-1400 (JEOL) microscope equipped with a LaB6 filament and operated at 120 kV. Images were recorded at a nominal magnification of 30,000-50,000x using a charge-coupled device camera (Gatan Orius SC1000B). For imaging at UCSF, samples were adsorbed onto 200-400 µM carbon-coated copper EM grids for 2-5 min at room temperature, blotted, and stained in 0.75% uranyl formate, blotted again, and allowed to air dry. Negative stain imaging was conducted with a Tecnai T12 microscope operating at 120 kV equipped with a Gatan Ultrascan CCD camera (Gatan, Pleasanton CA).

Electron Cryomicroscopy

For electron cryo-microscopy, 3.5 µl of the pelleted and resuspended liposome-nucleated $IST1_{NTD}$-CHMP1B copolymers were applied to glow-discharged Quantifoil holey carbon grids (2 µm hole size, 2-4 µm spacing, 200 mesh), blotted (7-9 seconds, -2 mm offset) and plunge-frozen in liquid ethane using a Vitrobot Mark I (FEI). To vitrify the membrane-remodeled samples, 3.5 µl of the pelleted and resuspended samples were applied to glow-discharged Quantifoil holey carbon grids (2 µm hole size, 2 µm spacing, 200 mesh), blotted (3-6 seconds, 0 mm offset, 100% humidity) and plunge-frozen in liquid ethane using a Vitrobot Mark III (FEI).

Electron cryo-micrographs were collected following low-dose procedures at liquid nitrogen temperature on one of four different microscopes: 1) a Tecnai TF20 operated at 200 kV (University of Utah), 2) a JEOL JEM3200FSC operated at 300 kV with an energy slit in-column filter of 20 eV (Baylor College of Medicine), and 3) a Titan Krios operated at 300 kV (OHSU/FEI Living Labs) and 4) a Tecnai Polara operated at 300 kV (UCSF). On the TF20 microscope, images were recorded at a nominal magnification of 50,000x on Kodak SO-163 film for 1 second with a total dose of ~10 e-/Å2. The developed film was digitized on a Zeiss Nikon Super Coolscan 9000 ED scanner. The final pixel size of the scanned images corresponded to 1.2 Å per pixel on the specimen level after calibrating the absolute magnification by analyzing 2D power spectra of catalase crystals imaged with the same microscope settings (39). On the JEM3200FSC microscope, images were recorded on a DE-12 direct electron detector (Direct Electron, LP) operating in movie mode at a recording rate of 25 raw frames per second for two seconds and for a total dose of ~20 e-/Å2. The first two frames and the last five frames were excluded, and frames 3-30 were aligned as whole frames using DE_process_frames.py. On the Titan Krios microscope, images were recorded without spherical aberration correction at a nominal magnification of 59,000x on a Falcon I direct electron detector for 1 second and a total dose of 10-15 e-/Å2. Images were recorded from ~0.6 to ~3.0 µm underfocus (fig. S2). Electron cryo-micrographs for the membrane remodeling reactions were collected following low-dose procedures at liquid nitrogen temperature on a Tecnai Polara. These images were recorded at a nominal magnification of 25,000x on a K2 Summit direct electron detector for 14 seconds and a total dose of ~60 e-/Å2 at ~2.0 µm underfocus.

Helical Reconstruction

Contrast transfer function parameters were estimated with CTFFIND3 (40). From 305 film negatives collected on the TF20 microscope, 61,168 particles were selected manually as overlapping segments using the EMAN2 program e2helixboxer.py (41) and saved as image stacks without in-plane rotation. The step between adjacent helical segments was at least one complete revolution of the helix (>51 Å), as judged from the raw images. Normalization and reference-free 2D classification were performed in RELION to identify structurally homogeneous subsets (figs. S1-2) (42). 2D classifications were run for 25-50 iterations with 50 classes at the original image size (340 square pixels, regularization parameter T=3).

58,104 (95%) of the starting film particles were classified into homogenous sets that corresponded to projections of a 1-start helix with varying degrees of out-of-plane tilt (fig S1). To determine the helical symmetry, we employed an extended version of the Iterative Helical Real Space Reconstruction (IHRSR) single particle algorithm as implemented in SPIDER (43, 44). From the properties of the 2D class averages of views orthogonal to the helical axis and parallel to the helical axis (fig S1) we estimated the helical symmetry to be ~21° of twist for ~3 Å of rise. Beginning with a featureless cylinder, the IHRSR algorithm converged on a twist of 21.06° and a rise of 2.96 Å.

We selected 118,467 particles from 2454 micrographs collected on the Titan Krios microscope and Falcon I direct electron detector and 12,142 particles from 39 micrographs collected on the JEM3200FSC microscope and DE-12 direct electron detector. These particles were interpolated and normalized with the RELION program relion_preprocess to have the same absolute pixel size (1.2 Å) as the particles collected on film, and subjected to the same reference-free 2D classification procedure described above. All particles from the combined TF20+film, Krios+Falcon I, and JM3200+DE-12 data that sorted into structurally homogenous 2D classes were subjected to 100 iterations of 3D classification in RELION with a regularization parameter of T=4. The final helical model determined using the IHRSR algorithm implemented in SPIDER was low-pass filtered to 60 Å resolution and used as the starting model for 3D classification. The 3D class that attained the highest resolution contained 114,286 particles, 79% of which were derived from the Krios+Falcon dataset, 18% of which derived from the TF20+film dataset, and 3% of which derived from the JM3200+DE-12 dataset. A final single-class "gold standard" auto-refinement procedure was performed within RELION, starting from a 60 Å low-pass filtered map of the helical polymer. Once the structure reached a nominal resolution of 10 Å, global searches were replaced by angular sampling of 1.8°, combined with local angular searches around the refined orientations.

The C1 3D reconstruction reached an asymmetric resolution of 7 Å at a Fourier Shell Correlation (FSC) cutoff of 0.5 according to RELION's implementation of gold standard FSC calculations to mitigate over-fitting (42). We note, however, that overlapping particles from single helical polymers were present in each of the random halves being compared, so the two half-maps were not truly independent. Nevertheless, we employed a resolution-limited refinement scheme within RELION so that particle orientations were determined using data only to 7 Å resolution. Upon convergence, 51 copies of the final half-maps were then transformed according to the helical symmetry operators, resampled on the grid of the original raw maps, and summed together using

UCSF CHIMERA (45). The final FSC curves for the averaged maps were calculated after multiplying a soft threshold-based mask to the two independent reconstructions. The final symmetric resolution estimate of 4 Å is a conservative interpretation according to the FSC = 0.143 criterion (fig. S3A) and the ResMap (46) local wavelet-based estimate (fig. S3B). The final combined density map was sharpened by a negative B-factor estimated using automated procedures implemented in the RELION program relion_postprocess(47).

Model Building and Refinement

Map segmentation: The density map was segmented with the Chimera (45) plugin Segger (48) using 4 steps of size 1 voxel with a cutoff of 0.13 voxels. After automated segmentation, adjacent segments were combined manually to preserve subunit connectivity.

Initial outer layer $IST1_{NTD}$ refinement: The $IST1_{NTD}$ crystal structure (3FRR) was idealized in Rosetta (49) and then relaxed while constraining the structure to the outer strand density. Iterative loop rebuilding was performed for 10 cycles, alternating between intensification and diversification. Loops to rebuild were selected based on the loops_from_density algorithm in Rosetta. Three copies of the best scoring structure were docked into the full map: the starting subunit, its lateral neighbor, and its longitudinal neighbor. These three subunits were used to determine the symmetry constraints using the make_symmdef_file.pl script from the Rosetta package with a contact cutoff of 12 Å and these constraints were used to refine one full outer strand ring in Rosetta. In the top scoring structures, a helical region between alpha 4 and alpha 5 (residues 136-142) appeared to be artificially flattened as a result of poorly resolved density. Helical constraints were added to this region and two cycles of loop rebuilding with constraints were performed to generate a final model.

We also considered the alternative possibility that the outer strand might comprise CHMP1B subunits. To address this question quantitatively, we generated a homology model for CHMP1B in the closed state (described in the following section). We then performed extensive real space refinements of both the closed-state $IST1_{NTD}$ and CHMP1B sequences against the outer strand asymmetric unit density. After first threading both sequences through the outer strand density, we perturbed the starting models randomly and performed hundreds of trials of model refinement using simulated annealing (starting temperature of 5000K). This approach produced ensembles of refined models for each subunit. Map-versus-model correspondence for the 100 lowest energy refined structures within the two ensembles were then scored using a real space correlation coefficient. This analysis demonstrated that the IST1 sequence agreed much better than the CHMP1B sequence with the outer-strand density because the mean correlation coefficient for the $IST1_{NTD}$ ensemble (0.67 ± 0.03) was significantly higher than for the CHMP1B ensemble (0.38 ± 0.07) , and the two ensembles of correlations did not overlap.

Initial inner layer CHMP1B refinement: A CHMP1B backbone model was manually built in Coot (50) based upon the inner layer density. The sequence was threaded onto the backbone and iteratively rebuilt by cycling between Rosetta rebuild and refine cycles, and manual rebuilding cycles in Coot. Three copies of the final rebuilt structure were docked into the full map: the starting subunit, its lateral neighbor, and its longitudinal

neighbor. The symmetry constraints were defined using the make_symmdef_file.pl script from the Rosetta package with a contact cutoff of 12 Å and, using these constraints, refined one full inner strand ring in Rosetta.

Heterodimer and full assembly refinement: The CHMP1B and $IST1_{NTD}$ layers were combined into a single pdb file. To refine the heterodimer structure within the context of the fully-assembled strands, we iterated between manual rebuilding and targeted real-space refinement (Coot) and fitting the structure to the density using MDFF (NAMD (51); CHARMM (52) protein force field as parameterized with VMD 1.9.1 (51, 53). After each cycle of rebuilding and refinement, the model was validated using Molprobity (54), and outliers were corrected by visual inspection and targeted regularization in Coot. Finally, Phenix.real_space_refine was used for refinement of the complete oligomer against the map (55, 56). Refinement runs included 10 macro-cycles of global gradient-driven minimization of $T = T_{data} + w*T_{restraints}$, where T_{data} is negated sum of map values at atom centers, $T_{restraints}$ is the geometry restraints term that includes standard restraints as well as secondary-structure restraints (57–59). Secondary structure annotation was performed manually. Relative weight w was optimized at each macro-cycle to achieve best model-to-map fit (highest Tdata value) such that rms deviations of covalent bonds and angles from ideal values do not exceed 0.01Å and 1 degree, correspondingly. Strict NCS (constraints) were used in refinement with the independent copy being the first two chains of $IST1_{NTD}$ and CHMP1B. Symmetry operators relating the copies were refined in parallel. Residue side chains were optimized using local grid search around rotatable chi angles in order to achieve best map fit while also adopting a valid rotamer state. The final refined model has excellent Molprobity scores (54, 60), and an above average EMRINGER score of 1.3 for a 4 Å resolution map (61).

Electrostatics: Electrostatic potentials were calculated from the final structure and for the $CHMP1B_{K107D,D155R}$ mutant using pdb2pqr (62) and the APBS software package (63).

Homology Modeling of CHMP1B in the Closed Configuration

To generate a homology model for the closed conformation of CHMP1B (residues 1 - 160), a diverse set of template structures was first identified using HHPred (64). The top structures were pdb entries 3FRT (CHMP3), 2GD5 (CHMP3), 3FRR (IST1), and 3GGY (IST1). The Rosetta comparative modeling protocol (65) was initialized with 7 different starting states: 2 alignments to 2GD5 (from HHPred server); 3 alignments to 3FRT (2 from HHPred server; 1 using PROMALS3D (66) and 1 alignment each for 3GGY and 3FRR (from HHPred). 5000 model structures for each alignment were generated and the 100 lowest energy structures were selected for further refinement. Iterative loop rebuilding was performed as described in (55, 65). Loops based on RMSF (Root Mean Squared Fluctuation) between starting structures were initially selected for rebuilding, followed by poorly folded regions identified manually. The structure was refined through alternating diversification cycles (in which results were clustered and the top scoring structures from each cluster were passed to the next cycle) and intensification cycles (in which only the top scoring structures were passed to the next cycle). 10-20 structures were propagated from one cycle to the next and cycles were continued until all helical regions appeared regular and well folded and the RMSD between the top 10 structures was less than 1.5 Å. Several regions had deviations from ideal helical geometry, which

were regularized by applying hydrogen bond distance restraints along the backbone in helical regions, followed by a short simulated annealing cycle using the molecular dynamics engine NAMD. The homology model was aligned to the extended state derived from the cryo-EM data and helix 5 did not align as expected. Since the position of helix 5 was somewhat variable during homology modeling and was well resolved in the cryo-EM data, the helix 5 region of the homology model was replaced by the equivalent region from the CHMP1B cryo-EM structure. MD simulations were performed to relax the connecting loop region. Solvent accessible surface area calcuations were performed in UCSF Chimera 1 and the pre-release version of Chimera 2.

Electron Cryotomography:

Vitrified samples of IST1-CHMP1B assemblies were imaged at 300 keV under low-dose conditions on a Titan Krios (OHSU/FEI Living Labs) transmission electron microscope with -8 μm defocus. Tilt series images were recorded while stepwise tilting the sample through +/- 60° in 2° increments. The cumulative electron dose per tilt series was limited to ~100 e-/Å2. All images were recorded on a Falcon I direct electron detector (FEI Company) at a nominal magnification of 59,000x resulting in a pixel size of 1.37 Å. The tilt series images were aligned and processed using IMOD (67) (The Boulder Laboratory for 3-D Electron Microscopy of Cells). Tilt series were aligned using gold fiducials and 3D volumes were reconstructed using 15 iterations of Simultaneous Iterative Reconstruction Technique (68) (Movie S5).

Cone Single Particle Image Processing:

4177 micrographs of SUV-free assemblies of full length IST1-CHMP1B were collected on a Titan Krios with a Falcon I detector at a nominal magnification of 59,000x, resulting in a pixel size of 1.37 Å. 9,954 cone images were selected manually using the EMAN2 program e2boxer.py and saved as image stacks. The original 680 square pixel images were 2x binned to 340 square pixels. Normalization and reference-free classification and class averaging were performed in RELION to identify structurally homogeneous subsets. 4,755 particle images were classified into one homogenous cone. A final gold standard auto-refinement procedure was performed within RELION, starting from a 60 Å low-pass filtered map of the cone. The 3D reconstruction of the asymmetric cone reached a nominal resolution of 25 Å (Figs. 4C, D and Movie S6).

Our reconstruction confirmed that the cones are composed of the same double-stranded filaments as those seen in the $IST1_{NTD}$-CHMP1B helices because: 1) the spiraling filaments are right handed, single start, and double-stranded; 2) each turn is separated by 5.1 ± 0.1 nm; 3) the narrow ends of the spiraling filaments taper to 24 nm, which matches the diameter of the $IST1_{NTD}$-CHMP1B helices; and 4) subunits at the tapered ends of the cones are related by ~21˚ rotation angles, which again matches the $IST1_{NTD}$-CHMP1B helices (fig S1).

Cell culture and Transfection:

U2OS and COS-7 cells originally derived from ATCC were cultured in DMEM (Invitrogen) with 10% FBS (Atlanta Biologicals, Atlanta GA). Cells plated on coverslips (#1.5 for immunofluorescence, #1 poly-L-lysine coated BioCoat coverslips (BD Biosciences, East Rutherford NJ) for EM) were transfected with the indicated plasmid(s)

using Lipofectamine 2000 (Thermo Fisher, Waltham MA) following the manufacturer's instructions and were used for experiments within 18–24 h.

Antibodies:

Antibodies used include rabbit polyclonal against CHMP1B (Proteintech, 14639-1-AP) and mouse monoclonal against c-myc (9E10, Developmental Studies Hybridoma Bank). Goat anti-rabbit and mouse secondary antibodies conjugated to Alexa 488 or 555 were from Molecular Probes (Thermo Fisher, Waltham MA) and the 12 or 18 nm gold were from Jackson Immunoresearch (West Grove, PA).

Immunofluorescence Microscopy:

Cells were fixed and stained essentially as described (21). Widefield epifluorescence imaging was performed using an OlympusIX81 microscope with 60x 1.42 NA objective and FLASH 2.8 camera (Hamamatsu Photonics). Brightness and contrast adjustments were made using Fiji (69).

Deep-etch Electron Microscopy:

Samples were prepared as previously described (17, 18). Briefly, coverslips were washed in 30 mM HEPES, pH 7.4, 100 mM NaCl, 2 mM CaCl2, dipped into an intracellular buffer (30 mM HEPES, pH 7.2, 70 mM KCl, 5 mM MgCl2, and 3 mM EGTA) and subjected to a brief pulse of ultrasound before transfer into the same buffer containing fixative (2% glutaraldehyde or 2% paraformaldehyde if immunostaining was planned). The area of coverslip with the highest yield of plasma membranes was identified by phase contrast microscopy and trimmed with a diamond knife to ~3 x 3 mm. Replicas were prepared as previously described (17, 18). Replicas were viewed on a JEOL 1400 transmission electron microscope at two different tilt angles (+/- 5°) and images were captured using an AMT XR111 camera. Digital image pairs were made into anaglyphs as described (70).

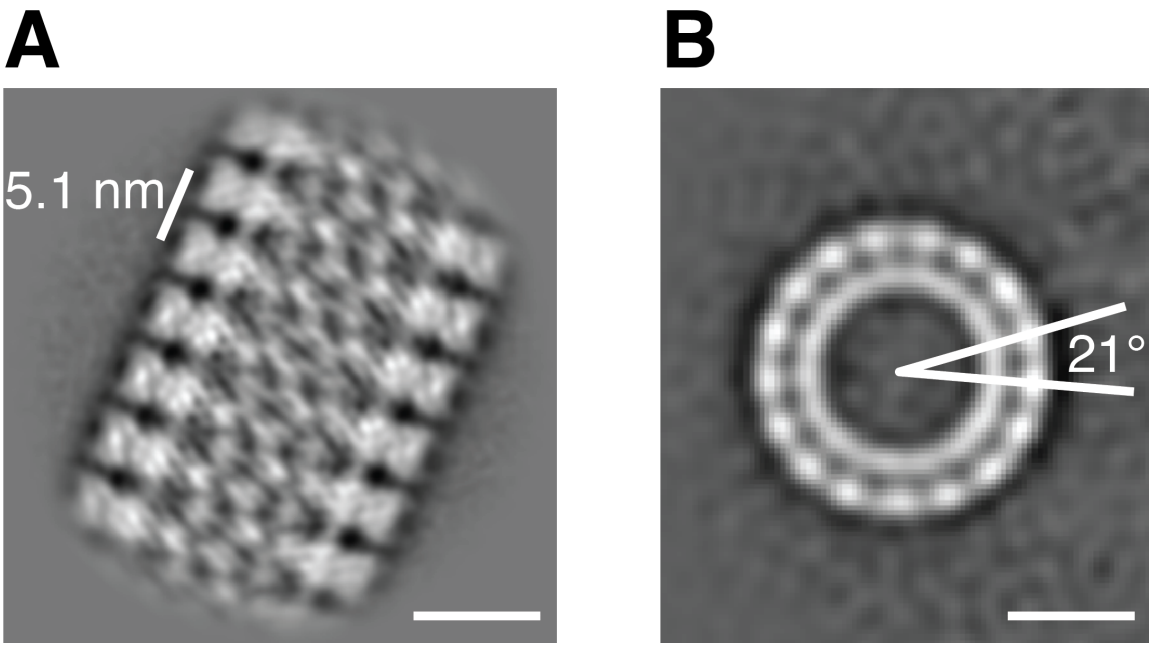

Fig. S1.

Helical symmetry estimation from 2D class averages: 2D class averages of the $IST1_{NTD}$-CHMP1B copolymer imaged orthogonal (A) and parallel (B) to the helical axis. These class averages revealed that the helix diameter is ~24 nm, the 360˚ repeat distance is ~5.1 nm (A), and the twist between adjacent subunits is ~21° (B). Bars: 10 nm.

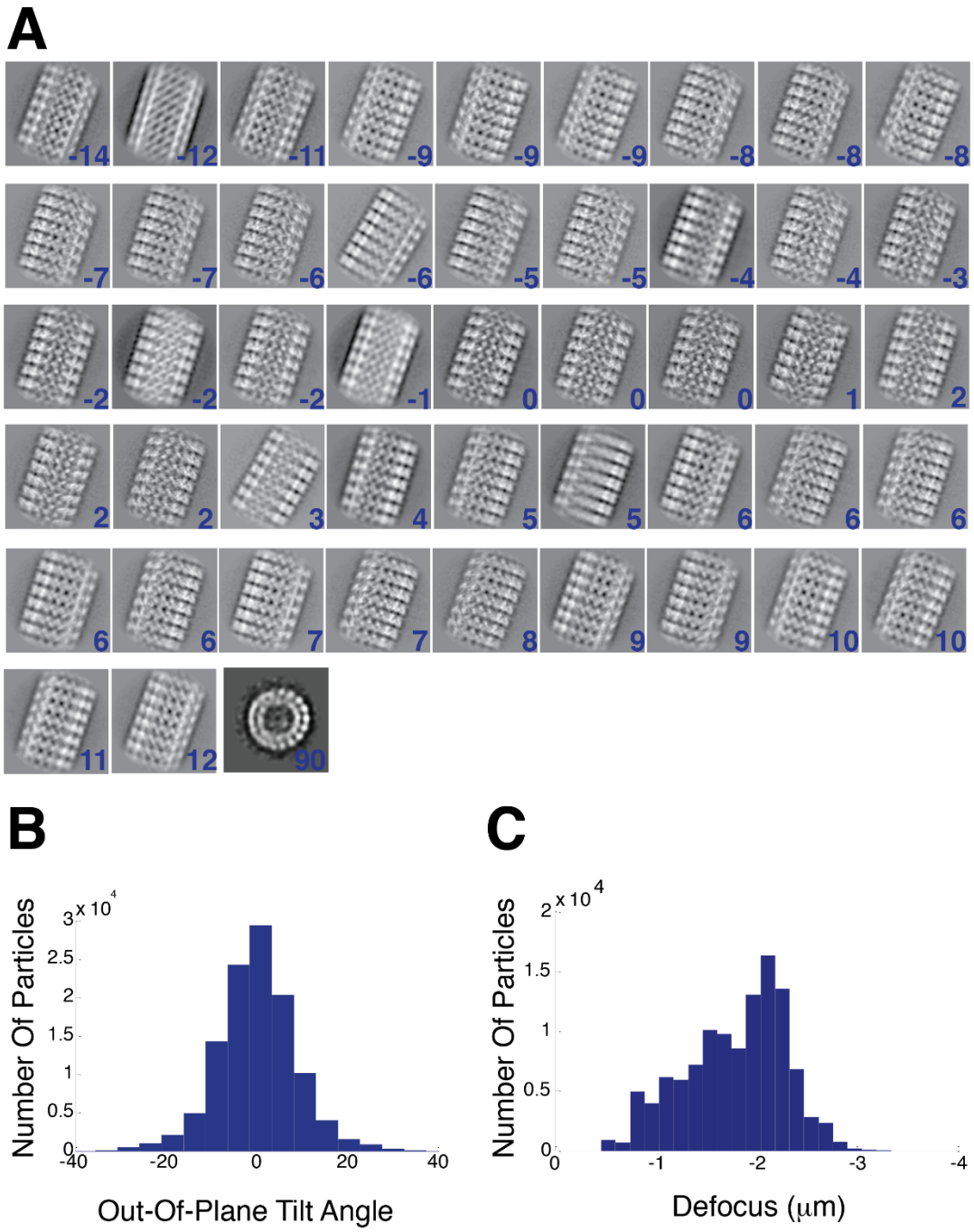

Fig. S2

2D classes, out-of-plane tilt and defocus values.
(A) 2D class averages of the IST1$_{NTD}$-CHMP1B copolymer arranged according to out-of-plane tilt angles (inset values) and a single end-on view 2D class average (90 degree tilt) as determined during the reconstruction process. (B) Histogram of out-of-plane tilt values determined during the reconstruction for particles included in the final single-class auto-refinement. (C) Histogram of defocus values, ranging from 0.75 μm to 3.2 μm, determined during the reconstruction for particles included in the final single-class auto-refinement.

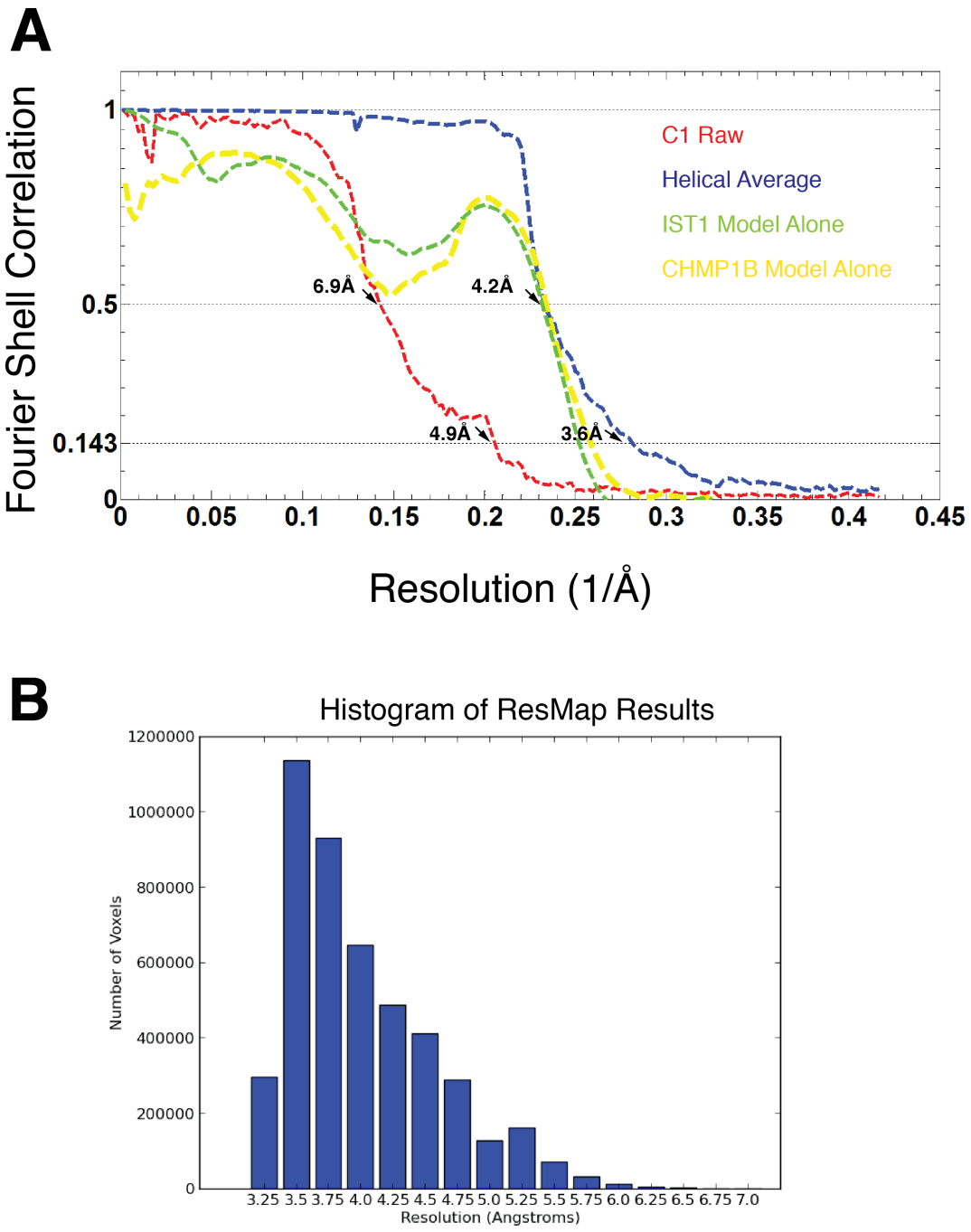

Fig. S3

Global and local resolution estimates for the IST1$_{NTD}$-CHMP1B reconstruction
(A) Fourier shell correlations (FSC) comparing two randomly assigned halves of the data prior to helical averaging (red curve), following helical averaging (blue curve), the IST1 atomic model alone (green curve) and the CHMP1B atomic model alone (yellow curve). (B) Histogram of voxels falling within ResMap (46) wavelet-based local resolution estimates, computed from 3.0 Å to 7.0 Å in 0.25 Å steps.

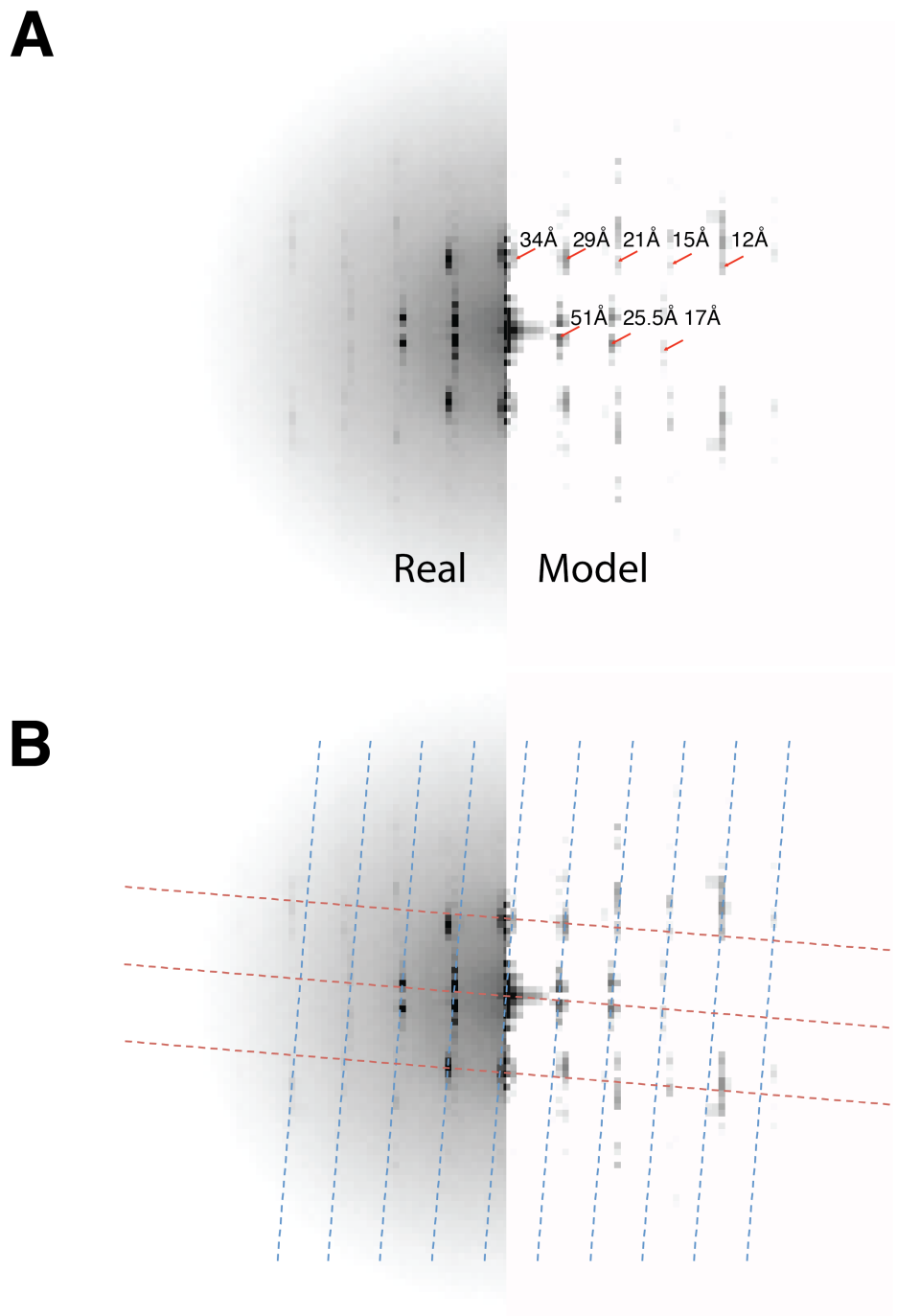

Fig. S4

Experimental versus model 2D power spectra

(A) Summed power spectrum generated from the helical segments used in the final reconstruction with <1˚ of out-of-plane tilt (left) compared with an untilted projection of the final reconstruction (right). The red arrows indicate layer line maxima at their respective at 1/Å positions. (B) The same power spectra as in (A) overlaid with a planar 2D lattice that corresponds with the layerline peaks observed for either the near or the far side of both the model and the experimental data.

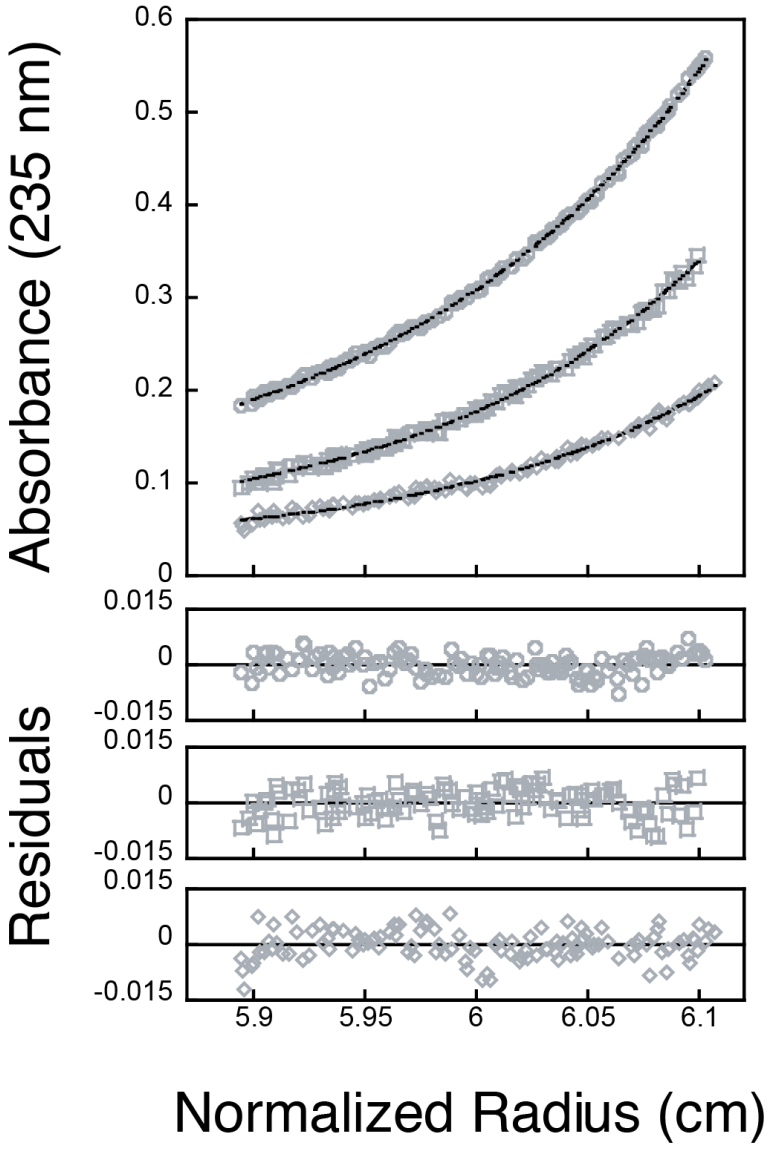

Fig. S5

CHMP1B is monomeric in high ionic strength solutions

Above: Representative equilibrium sedimentation distributions of pure recombinant CHMP1B in a high ionic strength buffer (20 mM NaPi, pH 7.0, 100 mM NaCl, 4 °C). Data are shown for CHMP1B centrifuged at 20,000 RPM at three different concentrations (1.6 mM, open circles, 800 μM, open squares, 400 μM, open diamonds). The global fits to single species models are also shown (solid lines), which included data from 200 μM CHMP1B, and from centrifugation rates of 12,000, 16,000 and 24,000 RPM (not shown for clarity). The experimentally estimated molecular weight (MWExp = 21,913 Da) agreed well with the molecular weight calculated for a monomeric protein (MWmonomer = 21,972; MWExp/MWCalc = 1.00). Below: residual differences between data and global fit.

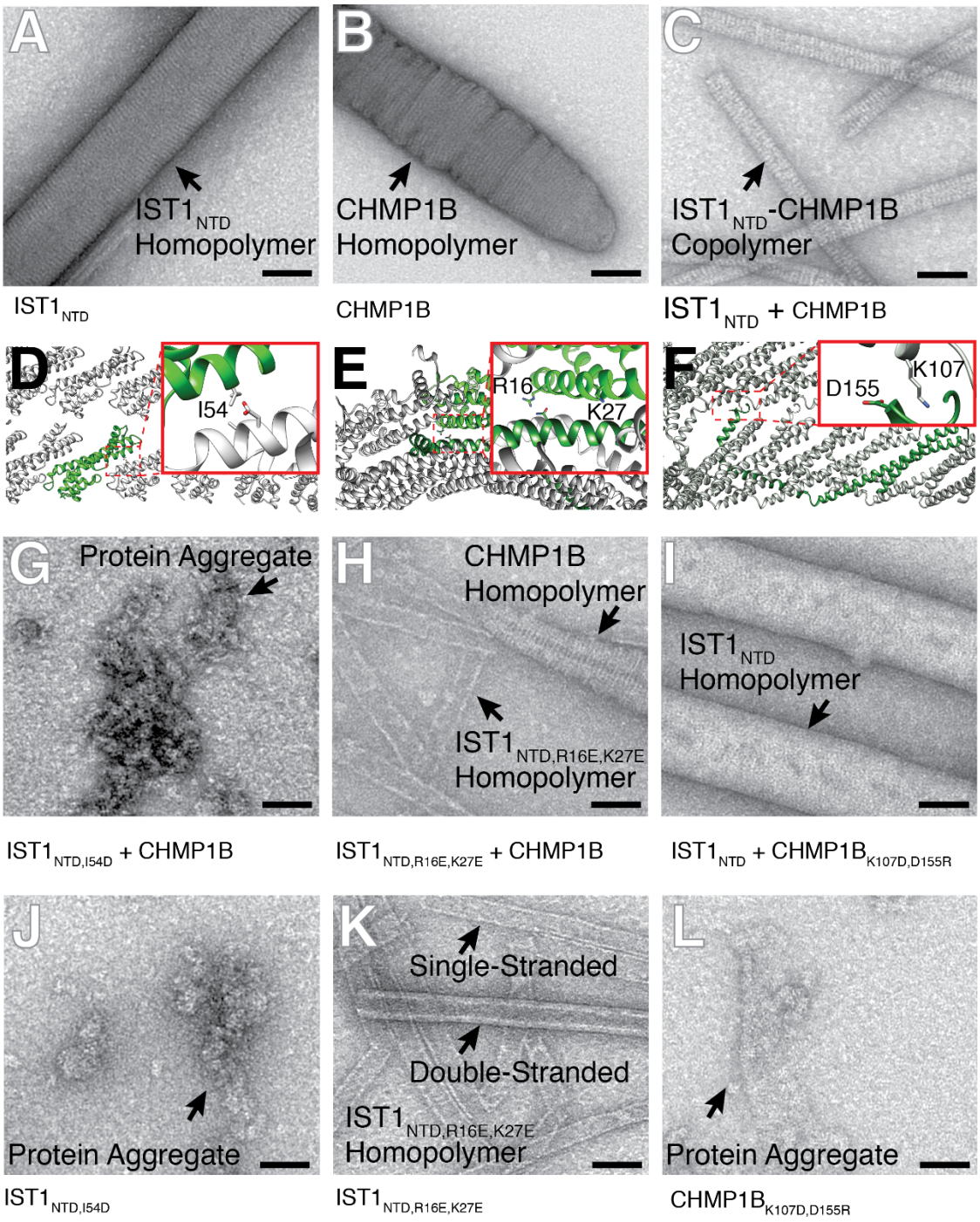

Fig. S6a

Mutational analyses confirm the importance of the different interfaces in the IST1$_{NTD}$-CHMP1B assembly

(A-C) Negatively stained electron micrographs of wild type IST1$_{NTD}$ homopolymer (A), CHMP1B homopolymer (B), and IST1$_{NTD}$-CHMP1B copolymers (C). The different tubes were readily distinguished based on tube diameters and striation patterns(4, 10). Note that our previous estimates of the IST1$_{NTD}$ and CHMP1B homopolymeric tube diameters (4)

were incorrect owing to a scaling problem and the correct widths are ~70 nm ($IST1_{NTD}$) and >90 nm (CHMP1B), with considerable heterogeneity. The different interfaces in the $IST1_{NTD}$-CHMP1B copolymer and the positions of mutated residues are shown in panels (D-F). Panels (G-I) show the consequences of mutating those residues on formation of $IST1_{NTD}$-CHMP1B copolymers, and panels (J-L) show the consequences of the mutations on formation of the relevant homopolymers. Panels (M-R) show the positions and lack of effects on $IST1_{NTD}$-CHMP1B copolymer formation for control mutations in residues that are not predicted to make important interface contacts.

Panels (D, G, J) test the importance of hydrophobic contacts between adjacent $IST1_{NTD}$ subunits along outer strand, formed between the N-terminal end of helix 2 and the C-terminal end of an adjacent helix 2. The importance of this interface for $IST1_{NTD}$-CHMP1B copolymer formation was tested using the $IST1_{NTD}$ Ile54Asp mutation ($IST1_{NTD,\ I54D}$). $IST1_{NTD}$ residue Ile54 resides near the N-terminal end of helix 2 and makes van der Waals contacts with helix 2 residues Asp77 and Leu78of the neighboring molecule. Consistent with the $IST1_{NTD}$-CHMP1B structural model, the IST1 Ile54Asp mutation blocked formation of regular $IST1_{NTD}$-CHMP1B copolymers, and only protein aggregates were observed in the co-assembly reaction (compare panels (G) and (C)). Panel (J) shows that the $IST1_{NTD\ I54D}$ mutation also prevented $IST1_{NTD}$ homopolymer formation. Our interpretation of these data is that the $IST1_{NTD}$ Ile54 residue makes interface contacts that are important for $IST1_{NTD}$-CHMP1B co-assembly, that this residue also blocks $IST1_{NTD}$ homopolymer assembly, and that the $IST1_{NTD,\ I54D}$ mutant protein dominantly inhibits CHMP1B homopolymer formation because it can still bind CHMP1B subunits.

Panels (E, H, K) test the importance of the extensive contacts between the inner and outer strands that involve the buried IST1 helix 1 (outer strand) interacting with three different CHMP1B subunits (inner strand). The importance of this interface for $IST1_{NTD}$-CHMP1B copolymer formation was tested using the $IST1_{NTD}$ Arg16Glu, Lys27Glu double mutation ($IST1_{NTD,\ R16E,K27E}$). $IST1_{NTD}$ residues Arg16 and Lys27 reside on the buried helix 1 of IST1 and make contact with two different CHMP1B residues across the strand interface. Consistent with the $IST1_{NTD}$-CHMP1B structural model, $IST1_{NTD,\ R16E,\ K27E}$ failed to co-assemble with CHMP1B (H), but in this case both $IST1_{NTD,\ R16E,\ K27E}$ and CHMP1B still formed separate homopolymers in the reaction mixture because this mutation disrupted only the interaction between the two strands. As expected, $IST1_{NTD,\ R16E,\ K27E}$ could still form homopolymers (K), although unlike the wild type protein the resulting tubes could apparently be either single- or double-stranded. Our interpretation of these data is that the Arg16Glu, Lys27Glu double mutation specifically inhibits $IST1_{NTD}$-CHMP1B interstrand interactions (consistent with the structural model).

Panels (F, I, L) test the importance of ionic interactions between adjacent filaments made through packing of positive patches from the N-termini and the helix 3/4 loops of both CHMP1B and $IST1_{NTD}$ against negative patches from the $IST1_{NTD}$ helix 1/2 and helix 5/6 loops (outer strand) and CHMP1B helix 5 (inner strand). The importance of this interface for $IST1_{NTD}$-CHMP1B copolymer formation was tested using the CHMP1B Lys107Asp, Asp155Arg double mutation ($CHMP1B_{K107D,\ D155R}$). CHMP1B Asp155 resides at the C-

terminal end of helix 5 and contributes to the acidic patches displayed in Fig 2C, while CHMP1B Lys107 resides just beyond the "elbow" near the N-terminal end of helix 4 and contributes to the basic patch displayed in Fig 2D. Panel (L) shows that the CHMP1B Lys107Asp, Asp155Arg double mutation, which may weaken the electrostatic interaction between adjacent turns of the helix, also prevented CHMP1B homopolymer formation. Our interpretation of these data is that ionic interactions between adjacent turns of the $IST1_{NTD}$-CHMP1B filament are also important for assembly.

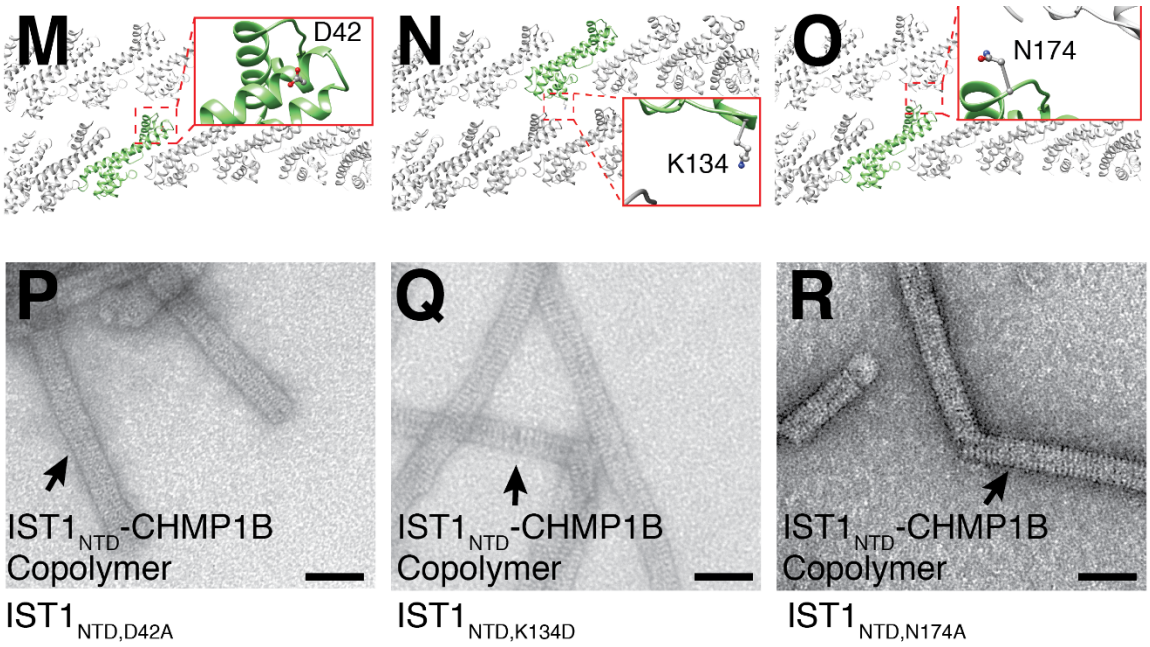

Fig. S6b

Mutational analyses confirm the importance of the different interfaces in the $IST1_{NTD}$-CHMP1B assembly (continued).

Panels (M-O) show the locations of three negative control, non-interface $IST1_{NTD}$ residues: Asp42 (M), Lys134 (N) and Asn174 (O). Consistent with the $IST1_{NTD}$-CHMP1B structural model, mutations in these residues did not inhibit $IST1_{NTD}$-CHMP1B assembly, as shown for $IST1_{NTD,\ D42A}$ (P), $IST1_{NTD,K134D}$ (Q) and $IST1_{NTD,\ N174D}$ (R). Bars: 50nm.

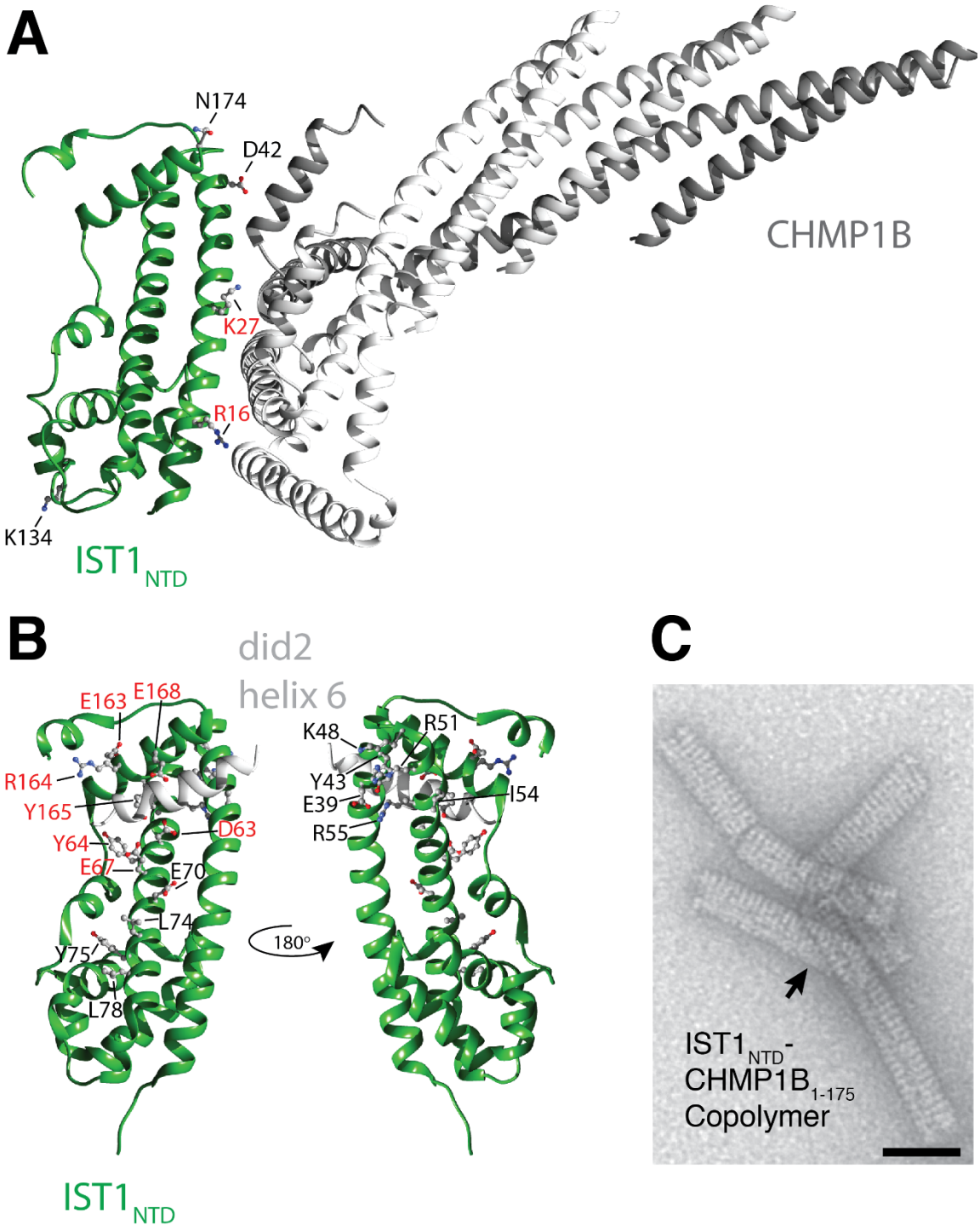

Fig. S7

Structural studies and mutational analyses reveal that IST1$_{NTD}$ and CHMP1B form structurally distinct heteropolymers and soluble binary complexes.
This figure summarizes the structural and mutational evidence that IST1$_{NTD}$ and CHMP1B can interact in two distinct ways: either forming the heteropolymers described in this study and illustrated in (A), or by forming the soluble, binary complex illustrated

in (B). We note that some of the same IST1 residues that are used to create the intermolecular interfaces in the $IST1_{NTD}$ co-polymer are also involved in crystal lattice contacts in previously published ESCRT-III crystals structures (e.g., I54 and surrounding residues), but none of the crystallographic protein-protein interactions match the geometry and symmetry of the $IST1_{NTD}$ interfaces seen in the co-polymer(4–6).

A) Overview of the co-polymeric interface between $IST1_{NTD}$-CHMP1B, highlighting key $IST1_{NTD}$ residues involved in co-polymer formation. Each $IST1_{NTD}$ subunit (green) interacts with three different CHMP1B subunits (different shades of grey). Interface residues shown to be important for copolymer assembly (fig. S6) are labeled in red. Non-interface control residues that were mutated but shown to have no effect on copolymer formation (fig. S6) are labeled black.

B) Overview of the distinct binary interaction formed between $IST1_{NTD}$ and the C-terminal helix of CHMP1B. To create the figures, the crystal structure of human $IST1_{NTD}$ (green, viewed as in (A)) was aligned with the crystal structure of yeast Ist1p (PDB: 3GGZ), in complex with CHMP1B (yeast Did2p) helix 6 (residues Asp188 to Gly204, shown in grey ribbon) (6). Residues shown explicitly were mutated and tested for effects on formation of the binary complex formed between human $IST1_{NTD}$ and helix 6 of human CHMP1B (4). Residues whose mutation reduced binding affinity more than 1.5-fold are labeled in red, and control residues whose mutation did not reduce binding affinity are shown in black. Note that the key IST1 binding residues all map to the crystallographically-defined binding site for helix 6 from yeast Did2p. Thus, the human and yeast Ist1 proteins appear to bind Chmp1B helix 6 in a similar fashion.

C) CHMP1B helix 6 is not required for $IST1_{NTD}$-CHMP1B co-polymer formation. Negative stained electron micrograph showing that a construct of CHMP1B lacking the C-terminal helix (CHMP1B1-175) co-polymerizes with $IST1_{NTD}$. Thus, the $IST1_{NTD}$-CHMP1B helix 6 interaction seen in the binary $IST1_{NTD}$-CHMP1B complex is not required for copolymerization. Bar: 50 nm.

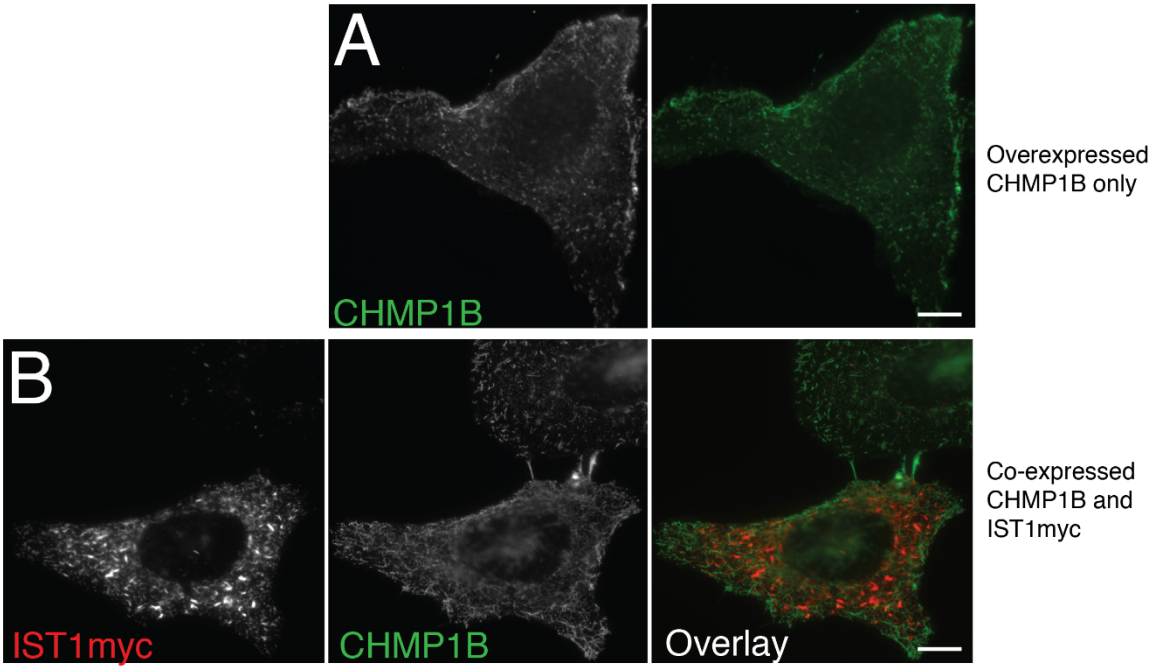

Fig. S8

Overexpressed CHMP1B and IST1 formed apparently tubular structures in cells. (A) Elongated CHMP1B structures in a U2OS cell expressing untagged CHMP1B. Comparable structures were observed with moderate to high expression of untagged or FLAG-CHMP1B. (B) U2OS cells co-transfected with CHMP1B and IST1-myc show that both proteins assembled into elongated and frequently tubular structures. Epifluorescence imaging, scale bar = 10 μm.

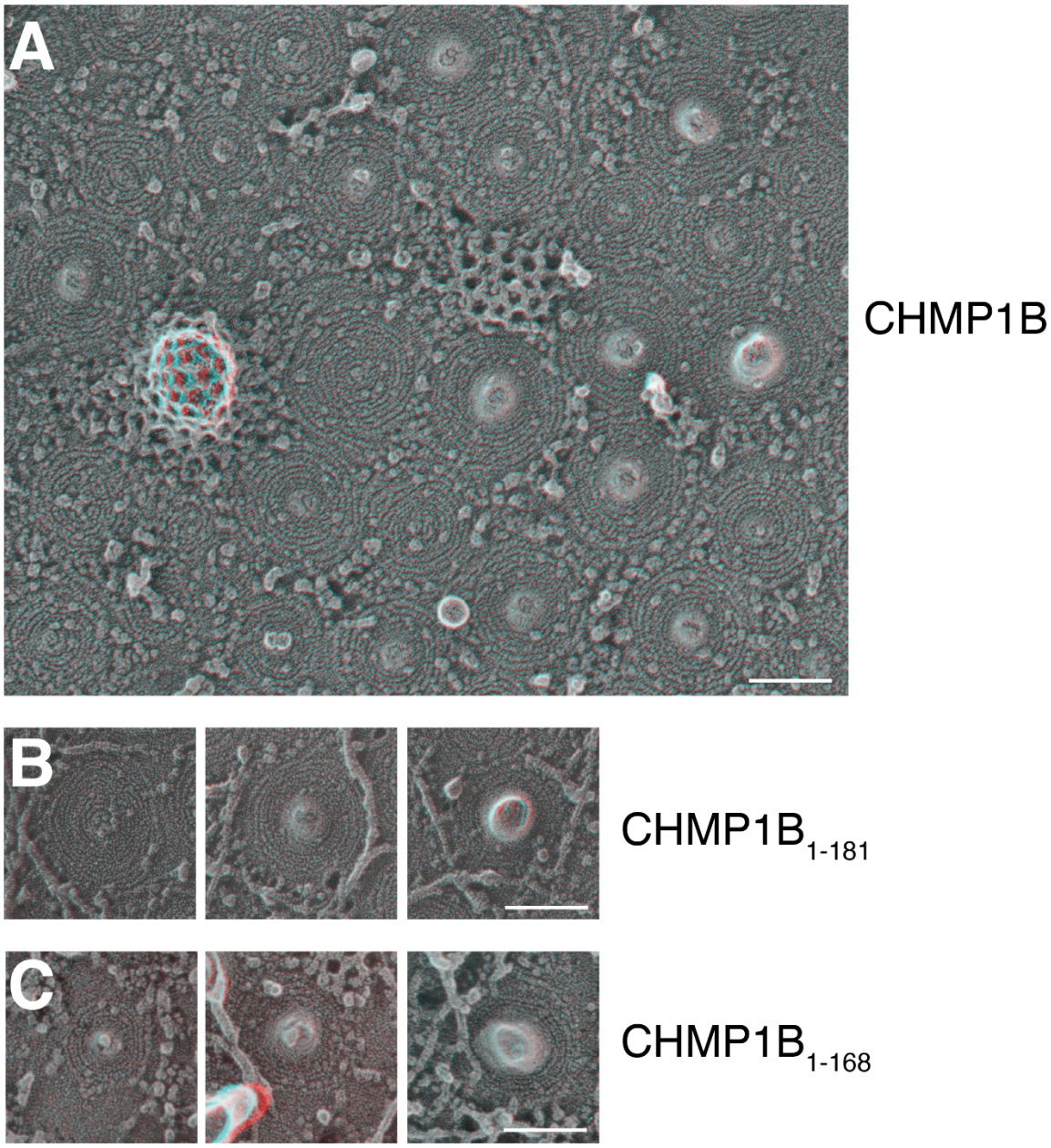

Fig. S9

Filament spirals formed by CHMP1B deletion mutants induce positively-curved membrane deformation.

(A) Survey view of filament spirals on the plasma membrane of a COS-7 cell expressing full-length FLAG-CHMP1B. (B and C) Filament spirals selected from COS-7 cells expressing FLAG-CHMP1B lacking indicated C-terminal sequences. Filament spirals are indistinguishable from those of full-length CHMP1B. Use view glasses for 3D viewing (left eye = red). Scale bars 100 nm.

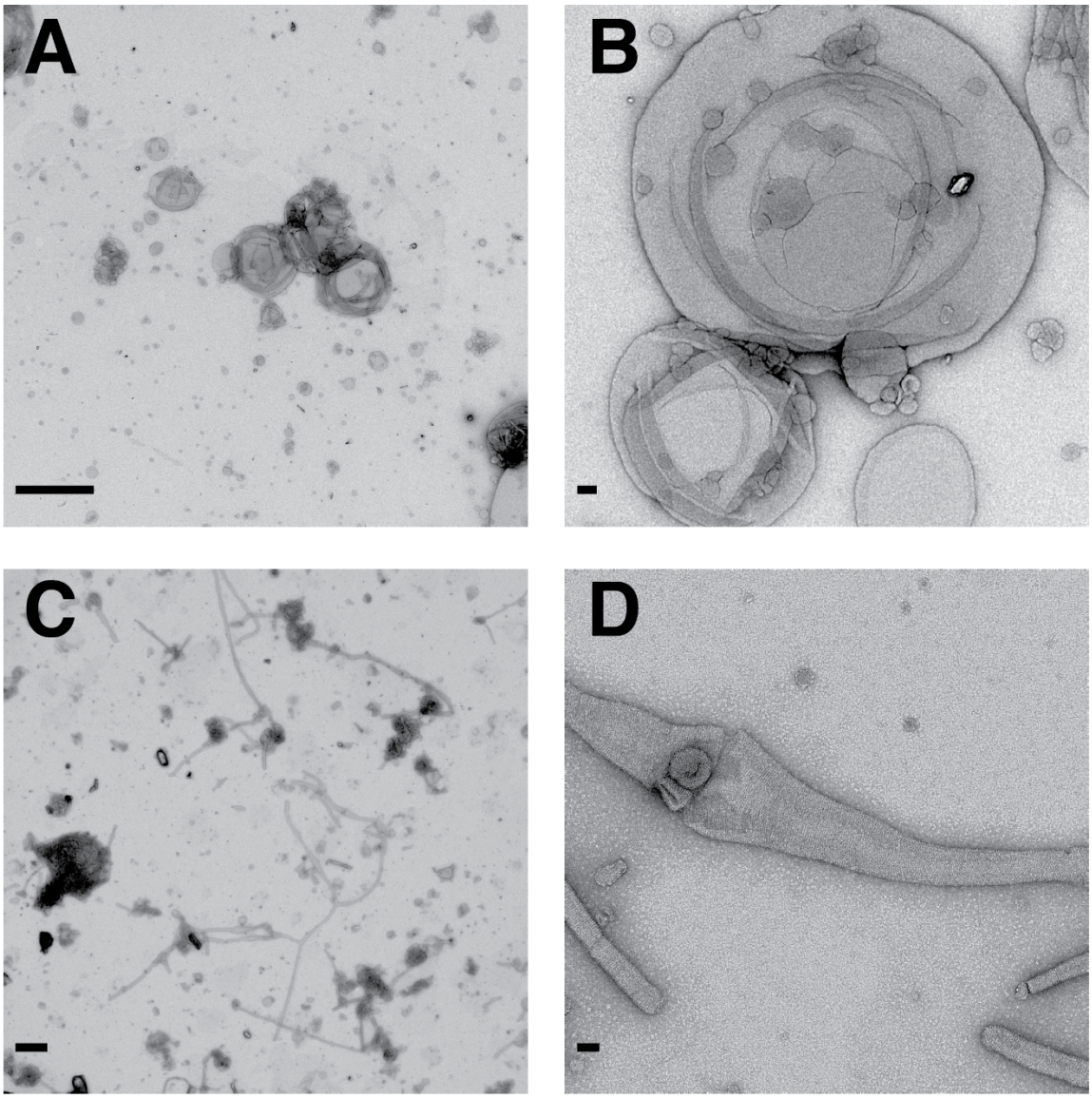

Fig. S10

Negative stain electron microscopy of membrane tubules induced by CHMP1B
Gallery of low magnification (left) and moderate magnification (right) images of large vesicles before (A,B) versus after incubation with CHMP1B (C,D). Bars: 1 μm panels A and C; 50 nm panels B and D.

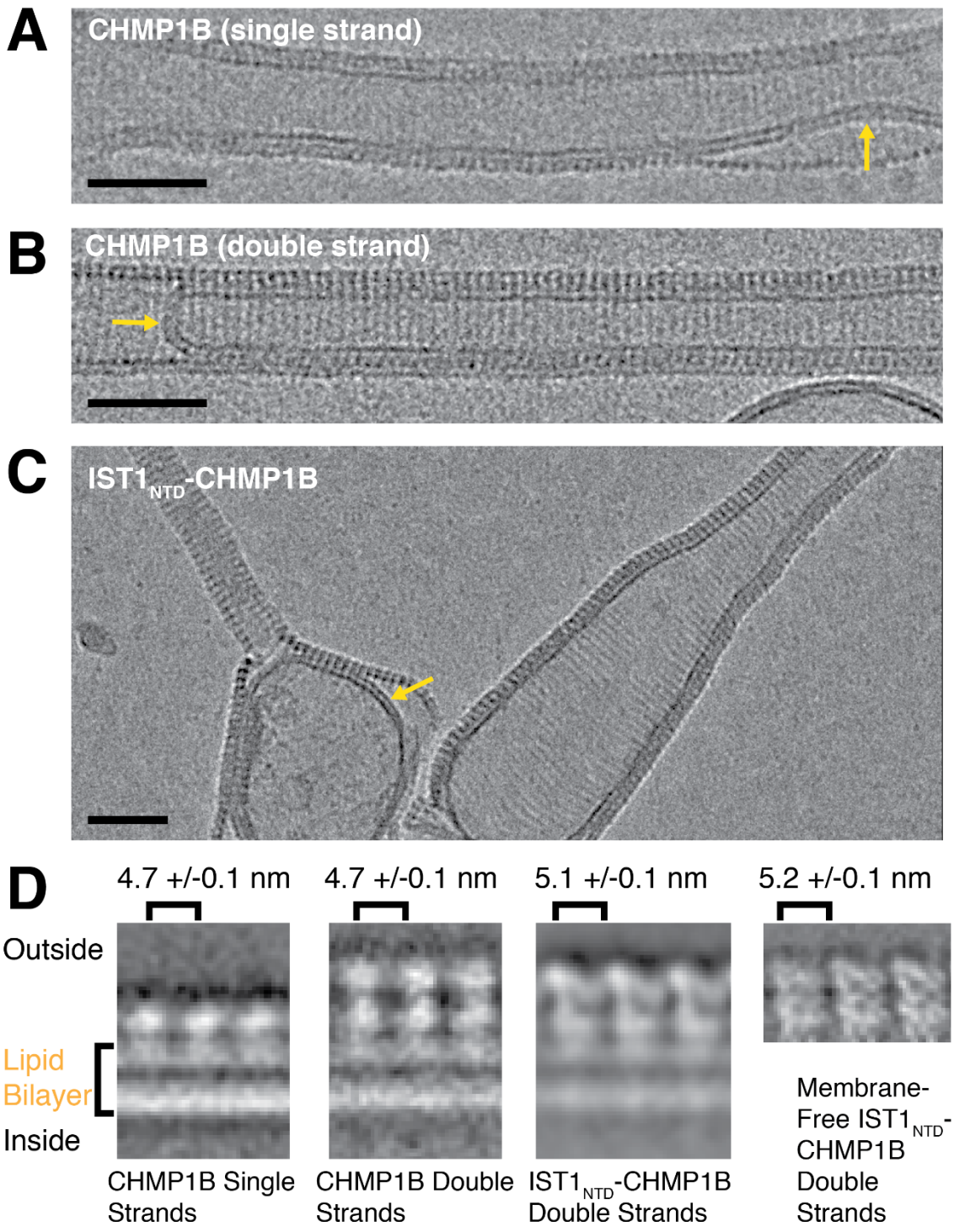

Fig. S11

Electron cryo-microscopy of membrane-bound CHMP1B and CHMP1B-IST1$_{NTD}$ copolymers.

Gallery of cryo-EM images and 2D class averages showing examples of membrane tubules surrounded by a single strand of CHMP1B (A), a double strand of CHMP1B (B), and double-stranded IST1$_{NTD}$-CHMP1B filaments (C). Comparisons of 2D Class

averages of cryo-EM images of tangential segments of membrane-bound assemblies showing (D) CHMP1B single strands (left), CHMP1B double strands (second from left), $IST1_{NTD}$-CHMP1B double strands (third from left), and one of the class averages from the reconstruction of membrane-free $IST1_{NTD}$-CHMP1B tubes (right, and see fig. S2). The interstrand spacing is indicated above each panel. The images and averages were selected to provide examples in which lipid bilayers (yellow arrows) can clearly be seen inside the protein coats. The relative frequencies of single- versus double-stranded CHMP1B coats formed in the absence of IST1 were single (52%) and double (41%) stranded CHMP1B coats (7% uncertain, n=12,097 single particle images). Bars: 50nm.

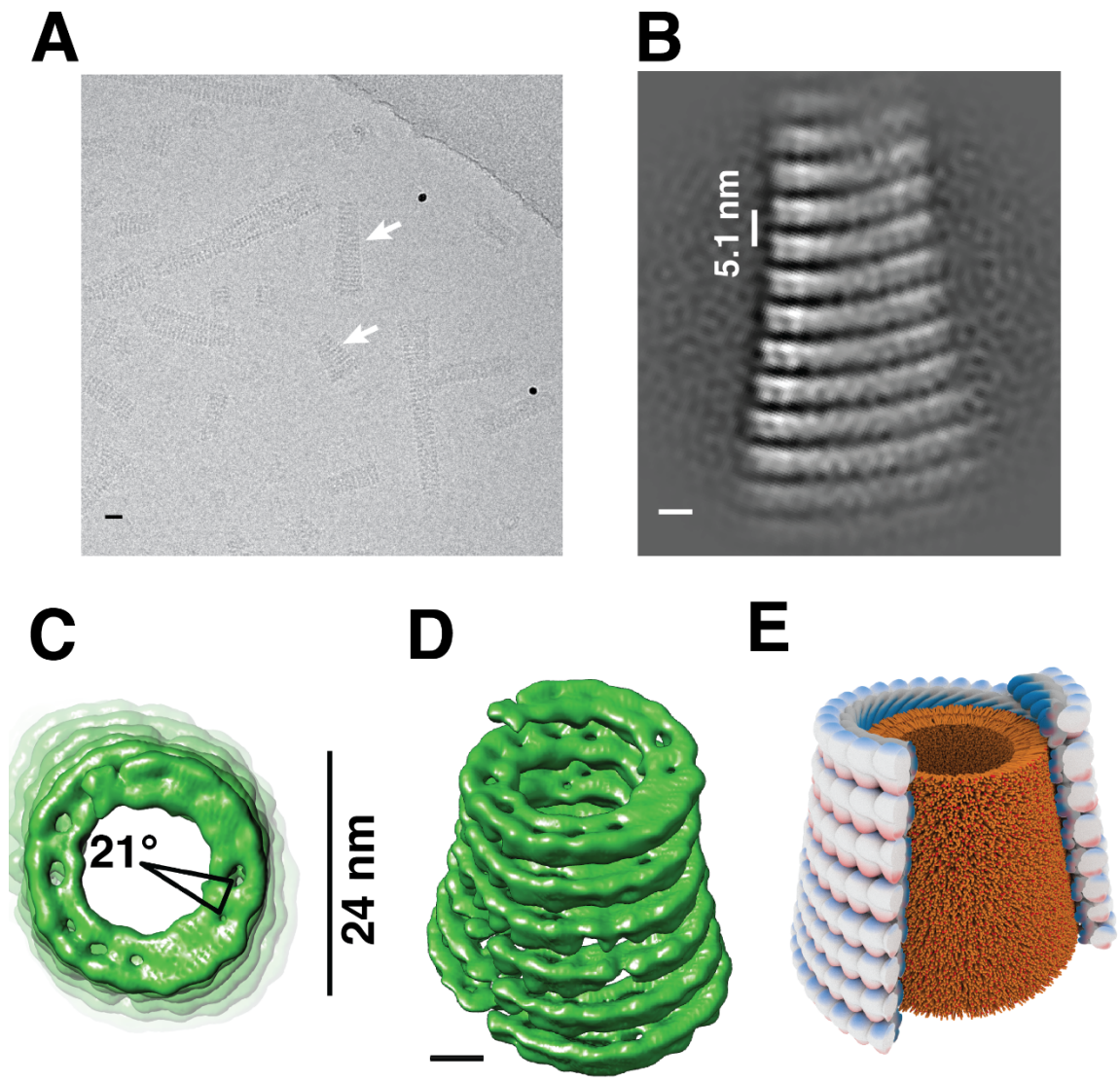

Fig. S12

Structure of IST1-CHMP1B conical spirals that constrict membranes.
(A) Electron cryomicrograph of IST1-CHMP1B assemblies formed by dialyzing equimolar (32 μM) IST1 and CHMP1B into a low ionic strength buffer in the absence of nucleating SUVs. Arrows highlight examples of conical spirals. (B) 2D class average of an IST1-CHMP1B cone. (C-D) 3D reconstruction of an IST1-CHMP1B cone. (C) End-on view of the narrow end of the cone showing the double-stranded character of the composite filament, the 21˚ rotation between subunits, and the 24 nm diameter. (D) Side view of the cone. Bar: 5.1 nm. (E) Model illustrating how IST1-CHMP1B spirals can constrict internal membranes. Dark blue: CHMP1B; light blue: IST1.

Table S1.
Refinement and Model Statistics

Real-Space Atomic Model Refinement Results	
rmsd (bonds):	0.01
rmsd (angles):	1.08
All-atom clashscore	8.69
Ramachandran plot:	
outliers:	0.00 %
allowed:	3.85 %
favored:	96.15 %
Rotamer outliers:	0.00 %
C-beta deviations:	0
EMRinger score:	1.3

Table S2.

Plasmid Name	Internal ID	Backbone	DNASU Plasmid ID	Epitope Tags	Source*/Comments
Bacterial Vectors					
pET16b IST1	WISP 07-72	pET16b, Novagen	HsCD00671538	N-term HIS	NP_001257904 [1]
pcDNA4/TO IST1		pcDNA4/TO		C-term Myc	NP_001257904
pGEX IST1 1-189	WISP 07-74	pGEX-2T-TEV	HsCD00520979	N-term GST	NP_001257904
pGEX IST1 1-189 $_{I54D}$	WISP 09-41	pGEX-2T-TEV	HsCD00520945	N-term GST	NP_001257904
pGEX IST1 1-189 $_{D42A}$	WISP 14-25	pGEX-2T-TEV	HsCD00671563	N-term GST	NP_001257904 [2]
pGEX IST1 1-189 $_{K134D}$	WISP 14-29	pGEX-2T-TEV	HsCD00672708	N-term GST	NP_001257904 [2][3]
pGEX IST1 1-189 $_{N174D}$	WISP 14-30	pGEX-2T-TEV	HsCD00671566	N-term GST	NP_001257904 [2][3]
pGEX IST1 1-189 R16E K27E	WISP 12-154	pGEX-2T-TEV	HsCD00671570	N-term GST	NP_001257904 [2]
pGEX CHMP1B	WISP 08-221	pGEX-2T-TEV	HsCD00520966	N-term GST	AAG01449 [4][5]
pGEX CHMP1B K34	WISP 14-04	pGEX-2T-TEV	HsCD00671543	N-term GST	AAG01449
pGEX CHMP1B $_{K107D\ D155R}$	WISP 14-08	pGEX-2T-TEV	HsCD00671560	N-term GST	AAG01449 [5]
pcDNA FLAG CHMP1B		pcDNA3.1 FLAG		N-term FLAG	NP_065145
pcDNA CHMP1B		pcDNA3.1		None	NP_065145
pcDNAFLAG CHMP1B(1-181)		pcDNA3.1 FLAG		N-term FLAG	NP_065145
pcDNAFLAG CHMP1B(1-168)		pcDNA3.1 FLAG		N-term FLAG	NP_065145
pcDNAFLAG CHMP4A (1-164)		pcDNA3.1 FLAG		N-term FLAG	NP_054888

*Source refers to NCBI Reference sequence, GenBank Accession number, or literature reference.

[1] IST1 cDNA was originally obtained from ATCC

[2] Silent mutation was introduced to remove an internal BamHI site: c162a

[3] Silent mutations were introduced to convey resistance to siRNA depletion: c495t; g498c; t501c

[4] CHMP1B cDNA was originally obtained from HeLa cDNA. Originally reported in

von Schwedler, U. K. et al. The protein network of HIV budding. *Cell* **114**, 701-713 (2003).

[5] The protein labeled "CHMP1B" contains a K34E substitution compared to the sequence given in this GenBank Accession number and was originally reported in von Schwedler, U. K. et al. The protein network of HIV budding. Cell 114, 701-713 (2003). Note that like IST1$_{1-189,}$ IST1$_{1-189,\ K34}$ also co-polymerized with CHMP1B (not shown).

Movie S1
Two and a half complete turns of the $IST1_{NTD}$-CHMP1B reconstruction density, highlighting an outer strand subunit (light green, $IST1_{NTD}$) and an inner strand subunit (dark green, CHMP1B).

Movie S2
Docking of the $IST1_{NTD}$ crystal structure (3FRR), and the final refined atomic model for the $IST1_{NTD}$ subunit into a segmented subunit from the outer strand cryo-EM density. The movie initially shows unsharpened EM density, then sharpened EM density, and then zooms in to show the density and model for $IST1_{NTD}$ helix 2, including side chains. The initial docking is with the $IST1_{NTD}$ crystal structure, and then shows the final refined structure. The major difference between the two structures involves remodeling of helix A to obtain a better fit to the density. This helix may be mobile because it makes a lattice contact in the 3D crystals (4), and is not well resolved in the EM density, as compared to the other helices.

Movie S3
Docking of the final refined de novo atomic model for the CHMP1B subunit into a segmented subunit from the inner strand cryo-EM density. The movie initially shows unsharpened EM density, then sharpened EM density, then the docking of the final refined model, and then zooms in to show the density for CHMP1B helix 2, including side chains.

Movie S4
Morph animation between the "closed" homology model of CHMP1B and the "open" structure from the reconstructed $IST1_{NTD}$-CHMP1B copolymer.

Movie S5
Filtered electron cryotomogram of IST-CHMP1B conical assemblies imaged under frozen-hydrated conditions. The conical assembly resolved in the bottom half of the field of view was used as a starting model for the single particle reconstruction shown in fig. S12C-D.

Movie S6
Single particle reconstruction of a continuous conical spiral of the IST1-CHMP1B copolymer, low-pass filtered to 25 Å. The conical spiral comprises the same double-stranded filaments reconstructed to high resolution because: 1) the spiraling filaments are right handed, single start, and double-stranded; 2) each turn is separated by 5.1 ± 0.1 nm; 3) the narrow ends of the spiraling filaments taper to 24 nm, which matches the diameter of the $IST1_{NTD}$-CHMP1B helices; and 4) subunits at the tapered ends of the cones are related by ~21˚ rotation angles, which again matches the $IST1_{NTD}$-CHMP1B helices (fig S1)."